International Journal of Heat and Mass Transfer 132 (2019) 631–642

Contents lists available at ScienceDirect

International Journal of Heat and Mass Transfer

journal homepage: www.elsevier.com/locate/ijhmt

Experimental and numerical investigation on shell-side performance of a double shell-pass rod baffle heat exchanger

Xinting Wang, Yunmin Liang, Yue Sun, Zhichun Liu, Wei Liu *

School of Energy and Power Engineering, Huazhong University of Science and Technology, Wuhan 430074, China

ARTICLE INFO

Article history:
Received 18 August 2018
Received in revised form 29 October 2018
Accepted 7 December 2018

Keywords:
Shell and tube heat exchanger
Rod baffle heat exchanger
Experimental investigation
Double shell pass
Guide shell

ABSTRACT

In this paper, the heat transfer and flow performance of a double shell-pass rod baffle heat exchanger (DS-RBHX) is investigated experimentally. Likewise, a single shell-pass rod baffle heat exchanger (SS-RBHX) is set as the control. Water serves as the working fluid both in the shell side and tube side. Experimental results indicate that the overall heat transfer coefficient of the DS-RBHX is higher than that of the SS-RBHX for all measurements. As the shell-side volume flow rate varies from 2.8 to 15.2 m^3/h, the shell-side heat transfer coefficient and pressure drop of the DS-RBHX increase by 33.5–54.0% and 34.0–74.3%, respectively. From the perspective of the comprehensive performance, the shell-side heat transfer coefficient of the DS-RBHX is 14.4–24.3% higher than that of the SS-RBHX under the same shell-side pressure drop. Consequently, it is proved that the DS-RBHX has better comprehensive performance compared with the SS-RBHX. On the basis of experimental results, numerical studies are conducted to analyze the shell-side behaviors of the DS-RBHX further. According to numerical results, three kinds of guide shells, arranged at the end of the sleeve, are proposed to reduce the flow dead zone in the shell-side outlet zone. The behaviors of DS-RBHXs with the guide shell (DS-RBHX-GSs) are obtained numerically. The results show that all three guide shells improve the heat transfer performance of the shell-side outlet zone, particularly in the outer side. Moreover, the guide shell of the DS-RBHX-GS2 has more significant effects than the others.

1. Introduction

Heat exchangers play a primary role in the industrial application, especially in the fields of power, energy, and chemical engineering. The shell and tube heat exchanger (STHX) is the most widely used heat exchanger owing to its high-pressure resistance, wide adaptability, simple manufacturing, and low cost [1]. Therefore, driven by the purpose of the energy-saving and emission-reducing, the heat transfer enhancement of STHXs is the research focus all over the world.

Many measures are taken both in the tube side and shell side of STHXs to enhance the heat transfer. For the tube side, generally, plain tubes are replaced by shaped tubes or tubes with inserts [2–4], whereas the situation of the shell side is more complicated deriving from its complex structure, vast size, and various baffles. For instance, the combined multiple shell-pass STHX was proposed and investigated using numerical and experimental methods by Yang et al. [5], which indicated that it was better on the overall performance than the conventional STHX with segmental baffles (STHX-SG). Wen et al. [6] developed a novel STHX with ladder-type fold baffles to eliminate the leakage in the conventional STHX with helical baffles (STHX-HB), and the experimental results revealed that the overall performance enhanced by 19.5% relative to the STHX-HB. Moreover, Tang et al. [7] contrived a novel connection method, named axial separation helical baffles, and their numerical results showed that the axial separation approach covered more application range than normal connection approach. El Maakoul et al. [8] compared the shell-side behaviors of the STHX-SG, STHX with trefoil-hole baffles, and STHX-HB, and the numerical results showed that trefoil hole baffles and helical baffles presented the best heat transfer and comprehensive performance, respectively, among three kinds of baffles. The porous model was adopted successfully on the investigation of STHXs with flower baffles by You et al. [9], and it was proved that it could accurately predict the heat transfer performance of STHXs via the comparison between the experimental and numerical results. In general, the heat transfer performance of STHXs is investigated experimentally and numerically. The two methods both have merits and drawbacks. Compared with the numerical simulation, the experiment is more accurate and widely approved, but it is extremely complex and time-consuming. The numerical simulation

* Corresponding author.
E-mail address: w_liu@hust.edu.cn (W. Liu).

https://doi.org/10.1016/j.ijheatmasstransfer.2018.12.046
0017-9310/

Nomenclature

A	heat transfer area (m^2)
B	systematic uncertainty
C_1, C_2, n	coefficients of Wilson plots
c_p	specific heat capacity ($J \cdot kg^{-1} \cdot K^{-1}$)
d	tube diameter (m)
D	random uncertainty
e	heat balance deviation (%)
F	LMTD correlation factor
h	heat transfer coefficient ($W \cdot m^{-2} \cdot K^{-1}$)
K	overall heat transfer coefficient ($W \cdot m^{-2} \cdot K^{-1}$)
L	effective tube length (m)
n	velocity exponent
N	number of shell passes
N_t	tube number
P	power consumption (W)
Δp	pressure drop (Pa)
q	heat flux ($W \cdot m^{-2}$)
Q	heat transfer rate (W)
R	heat resistance ($K \cdot W^{-1}$)
Re	Reynolds number
T	temperature (K)
ΔT_m	LMTD (K)
U	uncertainty
v	flow velocity ($m \cdot s^{-1}$)
V	volume flow rate ($m^{-3} \cdot s^{-1}$)
z	coordinate axis (mm)

Greek symbols

λ	thermal conductivity ($W \cdot m^{-1} \cdot K^{-1}$)

Subscripts

ave	average
i	inner side
in	inlet
o	outer side
out	outlet
ov	overall
oz	outlet zone
R, *x*, x_n	variables
s	shell side
t	tube side
w	tube wall

Abbreviations

CFD	Computational Fluid Mechanics
DS-RBHX	double shell-pass rod baffle heat exchanger
DS-RBHX-GS	double shell-pass rod baffle heat exchanger with guide shell
LMTD	logarithmic mean temperature difference
RBHX	rod baffle heat exchanger
SS-RBHX	single shell-pass rod baffle heat exchanger
STHX	shell and tube heat exchanger
STHX-SG	STHX with segmental baffles
STHX-HB	STHX with helical baffles

using CFD is the most prevailing research method for STHXs because of its convenience, less time-consuming, practicality, and simple operation [10]. Nevertheless, for complicated flows in the shell side of STHXs, it is quite difficult to obtain accurate results by CFD. Therefore, the combined use of experiments and simulations is the best methodology considering the time cost and accuracy.

It is universally known that the overall heat transfer coefficient of a given STHX depends on three parts: the shell-side heat transfer coefficient, the thermal conductivity of the tube wall, and the tube-side heat transfer coefficient. In the thermo-hydraulic experiments, it is the overall heat transfer coefficient that can be calculated directly via the measured variables, including temperatures and flow rates. Therefore, to evaluate the heat transfer performance of the shell-side, it is necessary to separate the shell-side heat transfer coefficient from the overall heat transfer coefficient through the data processing techniques. For a given STHX, the heat resistance of the tube wall is apparently constant. Consequently, the shell-side heat transfer coefficient can be calculated as long as the tube-side one is known. In the opening literature, many researchers used empirical correlations to calculate the tube-side heat transfer coefficient. Wen et al. [6] applied the Dittus-Boelter equation to obtain the tube-side heat transfer coefficient to compare the shell-side performance of STHXs with different baffles. Zhang et al. [11] and Gao et al. [12] both employed the Gnielinski equation to solve the tube-side heat transfer problems. Zhang et al. [13,14] used the fitting correlations obtained by previous tests by a modified Wilson plots to acquire the tube-side heat transfer coefficient of a finned tube. In some studies, however, the tube-side performance is the research purpose. Therefore, some empirical correlations were used to get the shell-side coefficient. For example, to obtain the thermo-hydraulic behaviors of the ice slurry in the tube side, Renaud-Boivin et al. [15] adopted the McAdams correlation to calculate the shell-side performance. Similarly, Farajollahi et al. [16] computed the shell-side heat transfer coefficient by Bell's procedure to obtain the heat transfer performance of nanofluids in the tube side. By the data processing method using empirical correlations, it can be found obviously that the shell-side heat transfer coefficient can be deduced by one overall heat transfer coefficient alone. It can dramatically reduce the test points of experiments. Therefore, it is widely used for the thermo-hydraulic experiments of STHXs. On the other hand, The Wilson plot [17] is another prevailing technique to evaluate the shell-side heat transfer coefficient from the overall heat transfer coefficient. Wilson pointed out that the tube-side heat transfer coefficient was proportional to the v_t^n, where the v_t is the tube-side flow velocity and the n is a known constant. The specific description about the Wilson plot is presented in Section 3.2. Peng et al. [18] and Jamshidi et al. [19] used Wilson plot to separate the shell-side one from the overall heat transfer coefficient. Fernandez-Seara et al. [20] summarized various Wilson plots which are suitable for different situations. If the Wilson plot is determined to be used in the data processing for the experiments of STHXs, many test points for different tube-side working conditions need to be completed to get one shell-side heat transfer coefficient. Therefore, the test points using the Wilson plot are a lot more than those using empirical correlations. Generally, compared with empirical correlations, the Wilson plot is considered to be more time-consuming, extensively applicable, and accurate.

Despite so many studies on STHXs, actually, STHX-SGs still occupy most of STHXs. However, they still have some drawbacks, including flow dead zones behind baffles, high pressure drop, and flow-induced vibration [21,22]. The rod baffle heat exchanger (RBHX) [23,24] was proposed by Phillips Petroleum Company to overcome the aforementioned defects [21,25]. Since then, RBHXs have attracted attention from researchers all over the world. Many

researchers devoted themselves to the heat transfer enhancement of RBHXs in the past decades. Smyth [26] reported that the RBHX slightly enhanced the heat transfer coefficient along with significant reductions of the pressure drop. Qiu et al. [27] summarized the reliable correlations for RBHXs via experiments to guide the design of RBHXs in the concentrating solar power system. To further enhance the heat transfer performance of RBHXs, most of the improvements were developed from the view of heat exchange tubes and rod baffles. For examples, plain tubes of RBHXs were replaced by spirally corrugated tubes [28], and rod baffles were substituted with novel plate baffles [29]. Nevertheless, the low flow velocity in the shell side is still one of the most primary barriers to the heat transfer enhancement of RBHXs. Therefore, Wang et al. [30] proposed a double shell-pass RBHX (DS-RBHX) in which a sleeve divided the shell side into two parts, as illustrated in Fig. 1. It was preliminarily concluded that the heat transfer performance of the DS-RBHX was improved dramatically compared with that of the single shell-pass RBHX (SS-RBHX) by numerical simulations.

To further evaluate the heat transfer performance of the DS-RBHX, the experiments are performed both for the SS-RBHX and DS-RBHX. The comparison of the shell-side performance between the two RBHXs is presented. Likewise, in order to eliminate the dead zone in the shell-side outlet zone, three novel guide shells are designed in the shell-side outlet zone, and their effects are studied numerically. The paper is outlined as follows: (1) The experimental setup is introduced in Section 2. (2) The procedure of the data reduction for performance parameters is depicted in Section 3. (3) Experimental results are compared and discussed in Section 4. (4) In Section 5, numerical studies are fulfilled to analyze experimental results further, and three DS-RBHXs with the guide shell (DS-RBHX-GSs) are proposed and investigated to enhance the heat transfer of the shell-side outlet zone. (5) Finally, several conclusions are summarized in Section 6. The improvement on the flow pattern is considered to be effective on the heat transfer enhancement of the DS-RBHX. Meanwhile, the present study is expected to promote the investigation on the multiple shell passes of RBHXs.

2. Experimental investigation

2.1. Geometric configuration

Two RBHXs, including a SS-RBHX and a DS-RBHX, are manufactured to compare their performance by experiments. The geometric models of two RBHXs are illustrated in Fig. 2. The two RBHXs are made up of 304 stainless steel to keep away from the corrosion. A sleeve and a partition are set in the shell side of the DS-RBHX. As listed in Table 1, the basic parameters of the two RBHXs are consistent, excepting the structure of baffles. The positions of nozzles are different to cater to the arrangement of baffles.

2.2. Experimental system

In this study, a test bench is designed to obtain the heat transfer and hydraulic performance of the water-water heat exchanger. As illustrated in Fig. 3, the experimental system consists of three parts, including the hot water loop, cold water loop, and test section. All pipes and tanks in this experimental system are made up of the stainless steel. The insulation covers all pipes and heat exchangers to avoid the heat loss.

The hot water loop comprises a hot water tank, two rotary flow meters, a frequency converter, and several water pumps. Several U-type heaters are set in the hot water tank. The heating power can be adjusted from 12 to 48 kW using a voltage regulator. The flow rate is controlled by a water pump with a frequency converter. The hot water flows through the tube side of the STHX from the hot water tank. After passing the heat exchanger to be tested, the working fluid flows back into the hot water tank driven by the water pump.

Via the pump and flow meter, the cooling water flows from a cooling water tank into the shell side of the STHX. The cooling water is heated in the STHX by the hot water in the tube side. Therefore, the refrigerating device, an air chiller, is employed to ensure a constant temperature in the cooling water tank. The cooling capacity can be regulated up to 56 kW by the control panel.

The test section is in charge of the data acquisition. Eight thermocouples and two differential pressure transmitters are arranged in the inlet/outlet nozzles of the STHX. All data are collected by the data acquisition system for the post-processing. Every thermocouple is calibrated via the calibrating furnace to ensure the high measurement precision. The test range and precision of measuring instruments are listed in Table 2.

2.3. Experimental procedure

The design of the experiment is completed first. The fifteen test points with different shell-side volume flow rates V_s are determined. Meanwhile, at least eight tube-side volume flow rates V_t are designated for one V_s. The operation parameters are adjusted as listed in Table 3 during the experimental period. The power of the heater and cooling capacity of the refrigerating device are adjusted to cater to each other. The test will not terminate until that the temperatures of the inlet/outlet nozzles are steady and the heat balance deviation e between the shell side and tube side

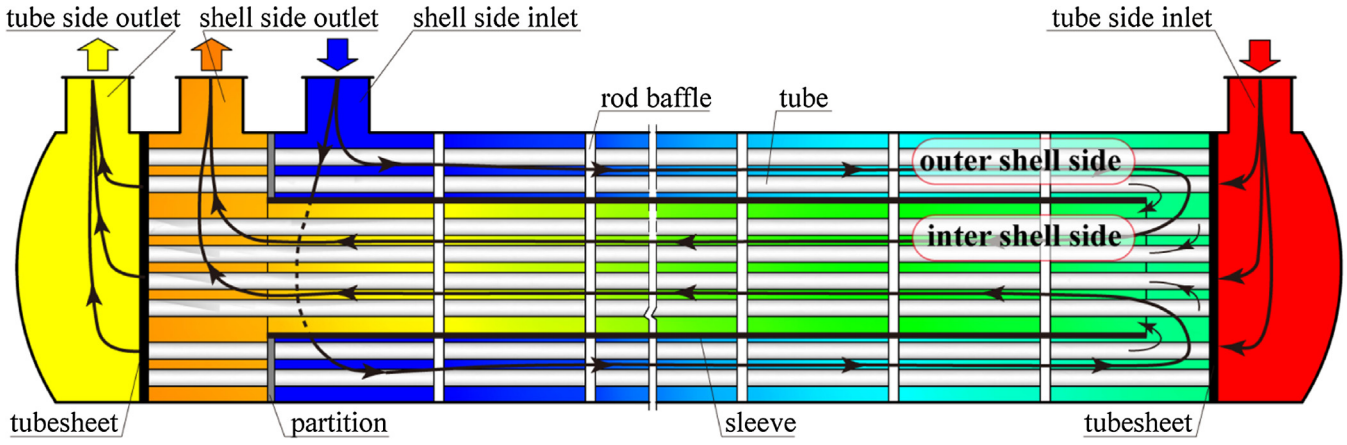

Fig. 1. Schematic diagram of DS-RBHX [30].

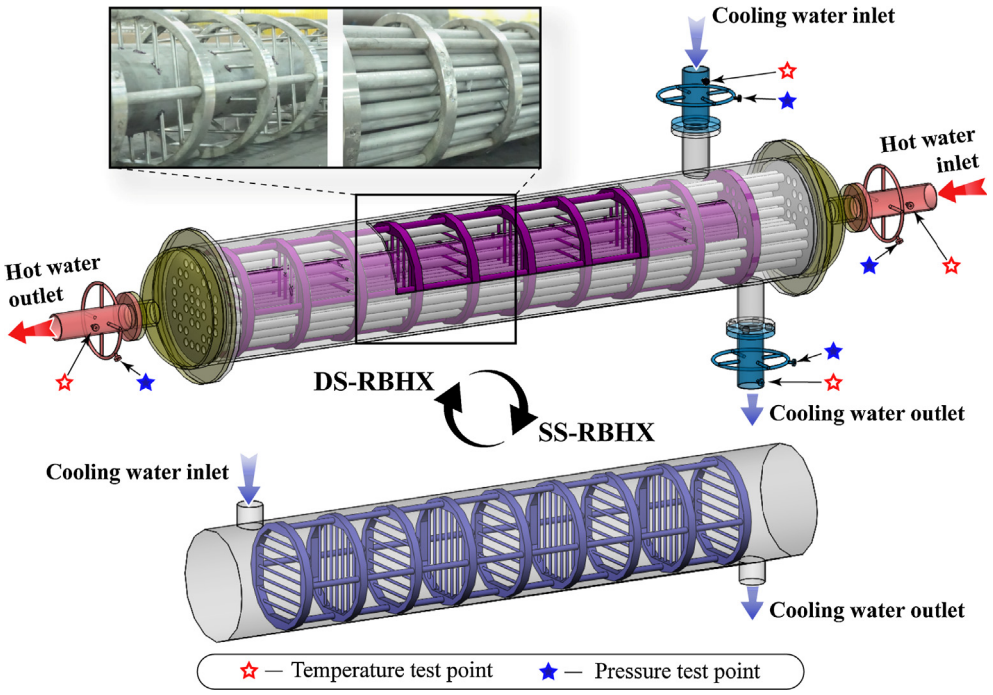

Fig. 2. Experimental models of SS-RBHX and DS-RBHX.

Table 1
Geometric parameters of experimental models.

Item	Value	
	SS-RBHX	DS-RBHX
Shell side (unit: mm)		
Inner/outer diameter	207/219	207/219
Inner diameter of inlet/outlet	50/50	50/50
Distance of inlet and tubesheet	80	218
Distance of outlet and tubesheet	80	80
Distance of partition and tubesheet	/	120
Thickness of partition	/	16
Inner/outer diameter of sleeve	/	93/103
Rod diameter	5	5
Rod baffle pitch	120	120
Inner/outer diameter of baffle ring	185/205	185/205
Thickness of baffle ring	16	16
Tube side (unit: mm)		
Inner/outer diameter	13/16	13/16
Effective length	1261	1261
Tube pitch	21.5	21.5
Tube number	40	40
Tube layout	Square	Square

can be controlled within 3%. The distribution of the heat balance deviations e is illustrated in Fig. 4 for all measurements.

3. Data reduction

In the present study, physical properties, such as the specific heat capacity, density, thermal conductivity, and dynamic viscosity, depend on the reference temperature of the working fluid. The average of inlet and outlet temperatures is determined as the reference temperature.

3.1. Overall heat transfer coefficient

The heat transfer rates of the shell side and tube side are calculated as Eqs. (1) and (2), respectively.

$$Q_s = M_s \cdot c_{p,s} \cdot (T_{out,s} - T_{in,s}) \tag{1}$$

$$Q_t = M_t \cdot c_{p,t} \cdot (T_{in,t} - T_{out,t}) \tag{2}$$

where M is the mass flow rate; T_{in} and T_{out} are the inlet and outlet temperatures, respectively; the subscripts s and t represent the shell side and tube side, respectively.

The average heat transfer rate Q_{ave} can be expressed as:

$$Q_{ave} = (Q_s + Q_t)/2 \tag{3}$$

In all experiments, the heat balance deviation e between the shell side and tube side, as defined in Eq. (4), is controlled within 3%.

$$e = |Q_s - Q_t|/Q_{ave} \times 100\% \tag{4}$$

The overall heat transfer coefficient K is defined as:

$$K = \frac{Q_{ave}}{F \cdot A_o \cdot \Delta T_m} \tag{5}$$

where ΔT_m is the LMTD of the counter flow; A_o is the outer area of tubes;

The ΔT_m and A_o are calculated as follows:

$$\Delta T_m = \frac{(T_{in,t} - T_{out,s}) - (T_{out,t} - T_{in,s})}{\ln\left((T_{in,t} - T_{out,s})/(T_{out,t} - T_{in,s})\right)} \tag{6}$$

$$A_o = N_t \pi d_o L \tag{7}$$

where N_t, d_o, and L are the number, outer diameter, and effective length of tubes, respectively.

F is the logarithmic mean temperature difference (LMTD) correlation factor [31], and it can be calculated as:

$$F = \frac{\sqrt{r^2+1}\ln\left(\frac{1-s}{1-rs}\right)}{(r-1)\ln\left(\frac{2-s\left(r+1-\sqrt{r^2+1}\right)}{2-s\left(r+1+\sqrt{r^2+1}\right)}\right)} \tag{8}$$

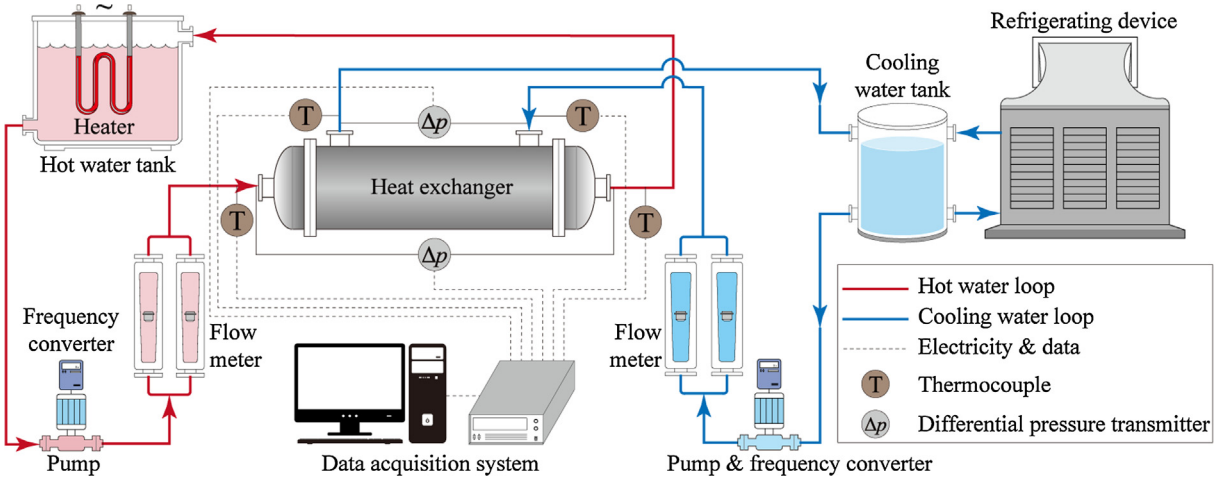

Fig. 3. Experiment system schematic.

Table 2
Test range and precision of instruments.

Instrument	Range	Accuracy
Thermocouple	−200 to 350 °C	0.3 °C
Flow meter	1–10 $m^3\ h^{-1}$	1.5%
Differential pressure transmitter	0–32 kPa	0.065%

Table 3
Ranges of operation parameters.

Operation parameters	Range
Shell side	
Volume flow rate/V_s, $m^3 \cdot h^{-1}$	2.8–15.2
Reynolds number/Re_s	1461–9578
Temperature of inlet/$T_{in,s}$, K	27.0–40.0
Tube side	
Volume flow rate/V_t, $m^3 \cdot h^{-1}$	2.8–14.4
Temperature of inlet/$T_{in,t}$, K	49.5–50.5
Reynolds number/Re_t	3349–18030

In Eq. (8), the r, p, α, and s are defined as:

$$r = \frac{T_{in,s} - T_{out,s}}{T_{out,t} - T_{in,t}} \tag{9}$$

$$p = \frac{T_{out,t} - T_{in,t}}{T_{in,s} - T_{in,t}} \tag{10}$$

For $r \neq 1$,

$$\alpha = \left(\frac{1 - rp}{1 - p}\right)^{1/N} \tag{11}$$

$$s = \frac{\alpha - 1}{\alpha - r} \tag{12}$$

where N is the number of shell passes.

3.2. Shell-side heat transfer coefficient and power consumption

The shell-side heat transfer coefficient is necessary to be parted from the overall heat transfer coefficient to characterize the shell-side performance. It can be separated by the Wilson plots [17,20] which is depicted as follows.

The overall heat resistance R_{ov} is defined as:

$$R_{ov} = R_t + R_w + R_s \tag{13}$$

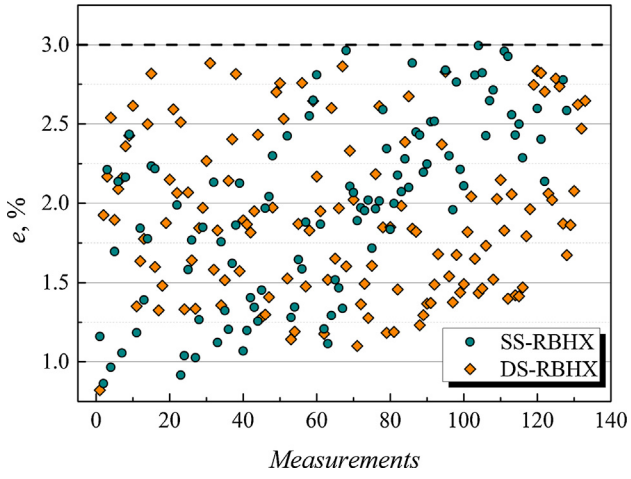

Fig. 4. Distribution of heat balance deviations.

$$\frac{1}{K} = \frac{1}{h_t}\frac{d_o}{d_i} + \frac{d_o}{2\lambda_w} \cdot \ln\frac{d_o}{d_i} + \frac{1}{h_s} \tag{14}$$

where λ_w is the thermal conductivity of the tube wall. It is set as a constant 15.2 $W \cdot m^{-1} \cdot K^{-1}$ for the stainless steel.

For a specific working condition, the shell-side heat transfer coefficient of the shell side h_s will be constant. Therefore, a constant C_1 is assumed as:

$$C_1 = \frac{d_o}{2\lambda_w} \ln\frac{d_o}{d_i} + \frac{1}{h_s} \tag{15}$$

According to Wilson's assumptions [17,20], the heat transfer coefficient of the fully turbulent single-phase flow inside a smooth tube h_t is the function of only the flow velocity v_t. The h_t can be described as Eq. (16).

$$h_t = C_2 \cdot v_t^n \tag{16}$$

Hence, the Eq. (17) is obtained basing on the Eqs. (14)–(16).

$$\frac{1}{K} = \frac{1}{C_2 v_t^n}\frac{d_o}{d_i} + C_1 \tag{17}$$

The Eq. (17) is a linear relation between $1/K$ and v_t^{-n}, where $n = 0.82$. Therefore, a straight line can be illustrated according to various tube-side flow velocities v_t. According to Eq. (15), the shell-side heat transfer coefficient h_s is calculated through the intercept C_1 of the straight line as Eq. (18).

$$h_s = \frac{1}{C_1 - \frac{d_o}{2\lambda_w}\ln\frac{d_o}{d_i}} \tag{18}$$

To evaluate the flow performance of the shell side, the power consumption is defined as:

$$P = \Delta p \cdot V \tag{19}$$

where Δp and V are the pressure drop and volume flow rate, respectively

3.3. Experimental uncertainty analysis

The experimental uncertainty is analyzed by the method depicted by Wheeler and Ganji [32]. The uncertainties of the measured variables, including the pressure drop, volume flow rate, and temperature, are expressed as:

$$U_x = \sqrt{B_x^2 + D_x^2} \tag{20}$$

where B_x is the systematic uncertainty; D_x is the random uncertainty.

The uncertainties of the result variables, to be a function of several measured variables, including but not limited to the heat transfer rate and overall heat transfer coefficient, are defined as:

$$U_R = \sqrt{\left(\frac{\partial R}{\partial x_1}U_{x_1}\right)^2 + \left(\frac{\partial R}{\partial x_2}U_{x_2}\right)^2 + \cdots + \left(\frac{\partial R}{\partial x_n}U_{x_n}\right)^2} \tag{21}$$

The experimental uncertainties of primary variables are calculated according to Eqs. (20) and (21), and they are listed in Table 4.

4. Results and discussion

4.1. Pressure drop

Fig. 5 compares the trend of the pressure drop along with the volume flow rate between the SS-RBHX and DS-RBHX. The pressure drop increases in pace with the increase of the volume flow rates both for two RBHXs. According to the comparison, we can clearly observe that the shell-side pressure drop of the DS-RBHX is about 34.2–74.3% higher than that of the SS-RBHX as the shell-side volume flow rate ranges from 2.8 to 15.2 m^3/h. Namely, the DS-RBHX will consume more pump power at the same volume flow rate compared with the SS-RBHX. The sleeve in the shell side of DS-RBHX causes the increase of the flow velocity, which results in the increase of the shell-side pressure drop. It is a negative change, but it is the evitable cost to improve the heat transfer performance.

4.2. Heat transfer performance

Fig. 6 shows the overall heat transfer coefficients of all measurements in the experiment. Theoretically, as defined in Eq. (14), the overall heat transfer coefficient is affected by the heat resistance of the shell side, tube side, and tube wall. Under our circumstances, the heat resistance of the tube wall is constant due to the fixed tube material and size. Therefore, the volume flow rates of the shell side and tube side, two of the measured variables, have marked

Table 4
Experimental uncertainties of primary variables of shell side.

Variables	SS-RBHX	DS-RBHX
K	±(4.58–11.83)%	±(4.55–9.92)%
Δp_s	±(0.80–3.50)%	±(0.35–2.57)%
V_s	±(1.26–4.82)%	±(1.26–4.82)%
Q_s	±(4.41–11.59)%	±(4.39–9.63)%

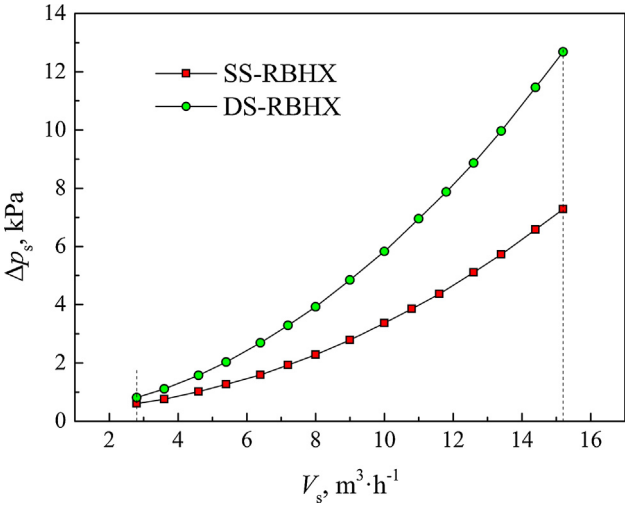

Fig. 5. Shell-side pressure drop versus volume flow rate.

effects on the overall heat transfer coefficient. From Fig. 6, the increasing volume flow rates of shell side and tube side both cause a monotonically increasing influence on the overall heat transfer coefficient. The overall heat transfer coefficient of the DS-RBHX is higher than that of the SS-RBHX under the same volume flow rate at any given test point. Therefore, it can be deduced preliminarily that the heat transfer performance of the DS-RBHX is superior to that of the SS-RBHX.

According to Wilson plots, the shell-side heat transfer coefficient is parted from the overall heat transfer coefficient. Moreover, its relationship with the shell-side volume flow rate has been illustrated in Fig. 7. Its behavior is similar to the overall heat transfer coefficient. The increment of shell-side heat transfer coefficient of the DS-RBHX, compared with that of the SS-RBHX, changes from 33.5% to 54.0% as the shell-side volume flow rate ranges from 2.8 to 15.2 m^3/h. Likewise, the increment gradually increases along with the increase of the flow rate. As a result, the DS-RBHX shows the better heat transfer performance relative to the SS-RBHX, especially in the working condition of the high shell-side flow rate.

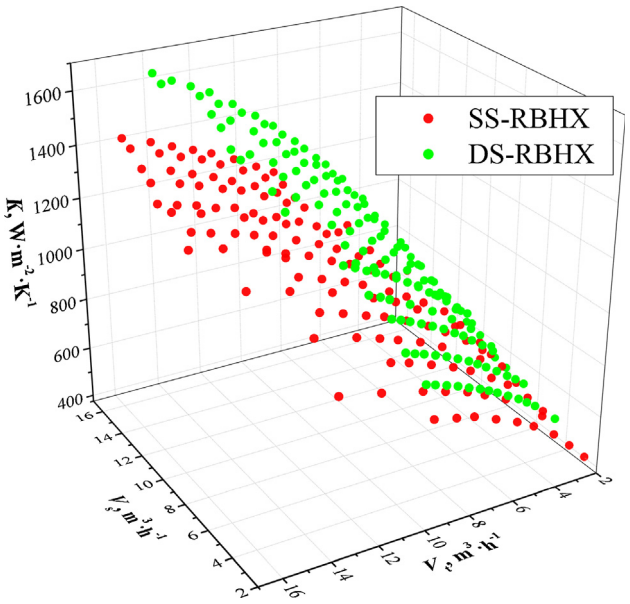

Fig. 6. Overall heat transfer coefficient versus volume flow rate of shell side and tube side.

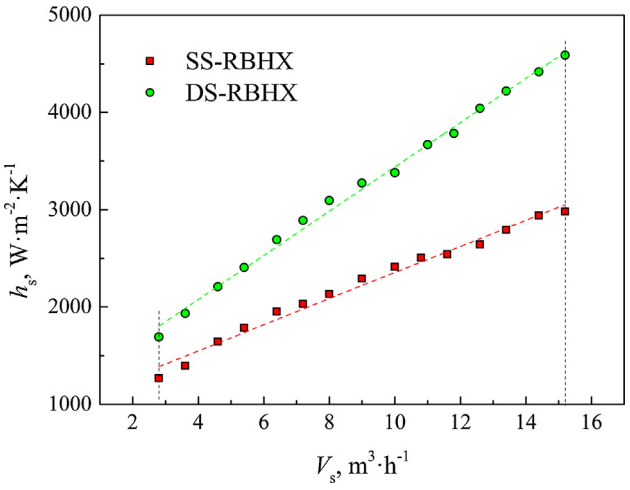

Fig. 7. Shell-side heat transfer coefficient versus volume flow rate.

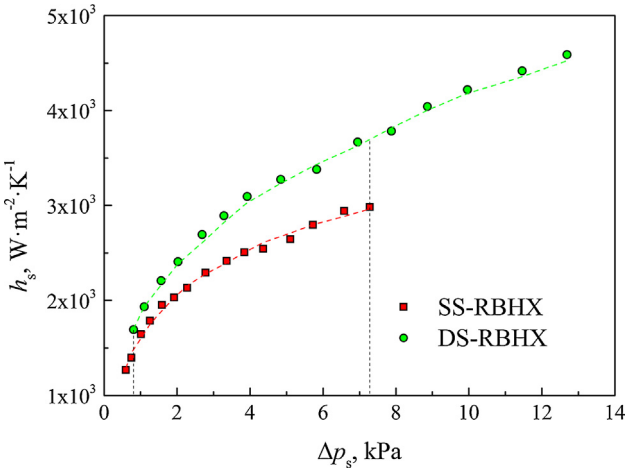

Fig. 8. Shell-side heat transfer coefficient versus pressure drop.

4.3. Comprehensive performance of shell side

Fig. 8 shows the relationship between the pressure drop and heat transfer coefficient of the shell side. Within the test scope, the shell-side heat transfer coefficient of the DS-RBHX is higher than that of the SS-RBHX under the same pressure drop. As the shell-side pressure drop ranges from 0.8 to 7.3 kPa, the shell-side heat transfer coefficient of the DS-RBHX rises by 14.4–24.3% compared with that of the SS-RBHX. The increment gradually increases along with the increasing of shell-side pressure drop. Therefore, the DS-RBHX has an advantage on the comprehensive performance of the shell side over the SS-RBHX. Likewise, the advantage has a progressive increase along with the increasing of the pressure drop Consequently, the DS-RBHX is pretty meaningful to improve the heat transfer coefficient and comprehensive performance of the shell side, especially under situations of high flow rates.

5. Performance study of DS-RBHX with guide shell in outlet zone

5.1. Numerical model

To dig out the performance of the DS-RBHX thoroughly, the numerical investigation is carried out using the commercial code Fluent for the shell side of the DS-RBHX. The 3-D, double precision, and pressure-based solver is employed to solve the steady problems. Practically speaking, the whole model of the shell side, which is more accurate than the periodic model and unit model for the numerical research on the shell side of the RBHX [33], is employed for all simulations. According to the comparison of different turbulent models for STHXs by Ozden and Tari [34], the realizable k-epsilon model is determined as the turbulent model. The standard wall functions serve as the near wall treatment. The inlet and outlet of the shell side are set as velocity-inlet and outflow, respectively. Only a part of experimental measurements, the shell-side volume flow rates ranging from 10 to 15.2 m^3/h, are included in the numerical studies, considering that the realizable k-epsilon turbulent model is more effective and precise on high-Re situations. The turbulent kinetic energy and turbulent dissipation rate of the velocity-inlet are calculated according to Ref [35]. Three grid systems with 1.3 mm, 1.5 mm, and 1.8 mm element sizes are generated to fulfill the mesh dependence test. The grid system with 1.5 mm element size is adopted for all numerical calculations considering the balance between the workload and accuracy. The mass flow rates of the shell-side inlet and outlet, the temperature of the shell-side outlet, and the total surface heat flux of tube walls are monitored during iterations. After iterations ending, the residuals of the momentum, turbulent kinetic energy, and turbulent dissipation rate are controlled within 5×10^{-4}, while that of the energy is within 5×10^{-7}. Moreover, the calculation will not stop until all residuals and monitored variables keep constant. The other settings keep consistent with those in the previous work [30].

As can be seen in Fig. 1 and Fig. 2, there is a sudden expansion when the working fluid flows from the inner shell side to the shell-side outlet zone. The fluid is inclined to flow into the outlet nozzle directly instead of washing the tubes arranged in the outer side of the outlet zone. Fig. 9 shows the path lines and velocity distribution of the outlet zone obtained by the numerical calculation. The flow velocity of the inner side and that near the outlet nozzle are larger than that on the opposite of the outlet nozzle. The flow dead zone is generated in the outer side of the outlet zone. Therefore, we can preliminarily deduce that eliminating the flow dead zone will be effective and meaningful to enhance the heat transfer of the outlet zone.

5.2. Physical model

On the basis of the analyses described above, three guide shells are proposed to enhance the disturbance and eliminate the flow dead zone of the outlet zone. The geometric structures and dimensions of four DS-RBHXs are illustrated in Fig. 10. Fig. 10(a) shows the structure of the original DS-RBHX, set as the control, without the guide shell. The DS-RBHXs with the cylindrical guide shell, guide shell with one rectangular opening, and guide shell with rectangular openings are numbered and depicted in Fig. 10(b)–(d), respectively. A cylindrical guide shell, widely applied in the inlet zone of STHXs, is arranged at the end of the sleeve in the DS-RBHX-GS1, which makes the working fluid flow along the guide shell. The guide shells in the DS-RBHX-GS2 and DS-RBHX-GS3 play the same role with that in the DS-RBHX-GS1. The opening of the guide shell in the DS-RBHX-GS2 leads the fluid to flow to the opposite direction of the outlet nozzle. Meanwhile, the guide shell with rectangular openings in the DS-RBHX-GS3 serves as a diverter to guide the fluid flow to various directions evenly. Heat exchange tubes are omitted to present the structure of guide shells clearly in the Fig. 10. The flow area in the guide shell is set at an intermediate value, 81.3 cm^2, of flow areas of the inner side and outer side. Effects of guide shells on the outlet zone and whole shell side are compared by numerical method hereinafter.

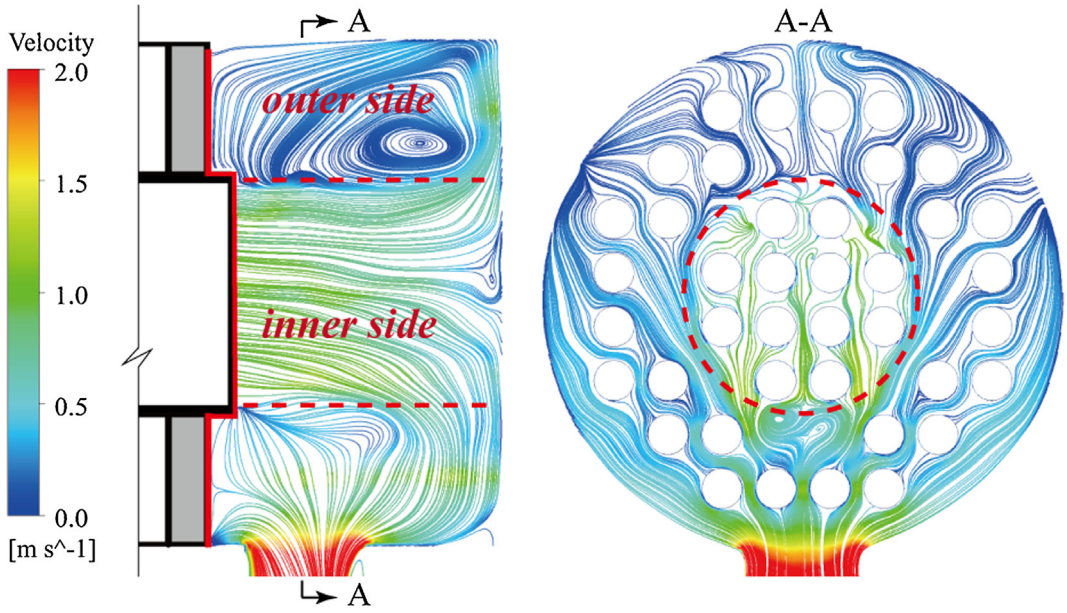

Fig. 9. Path lines and velocity distribution in outlet zone of DS-RBHX.

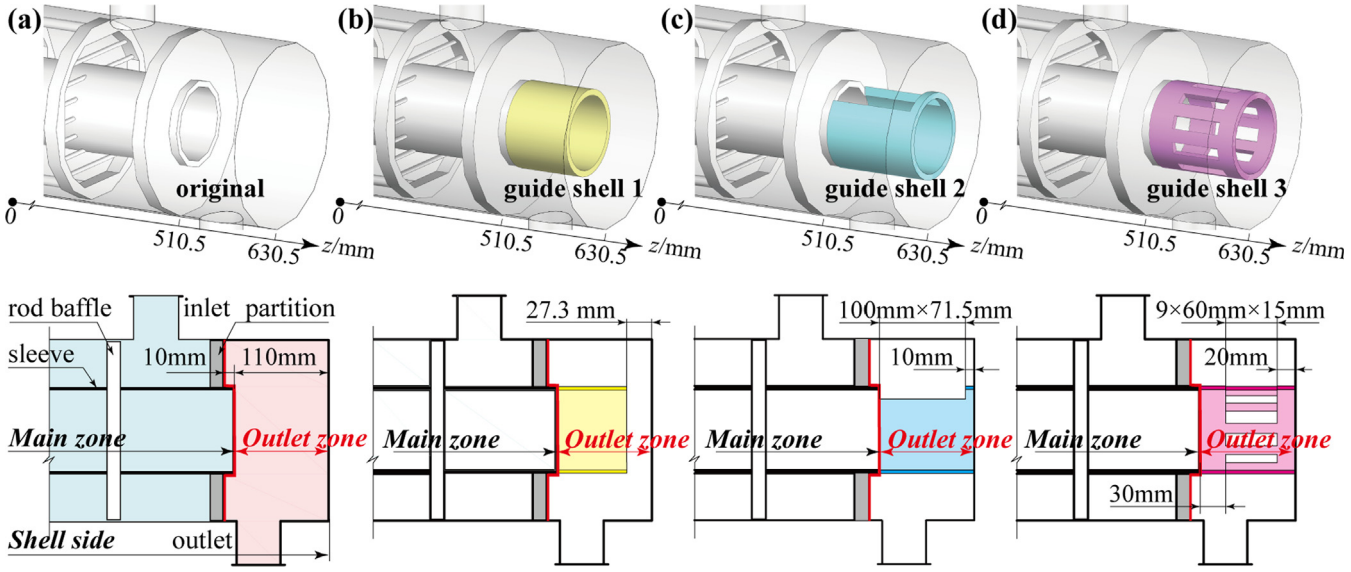

Fig. 10. Geometric diagrams of four DS-RBHXs: (a) DS-RBHX; (b) DS-RBGX-GS1; (c) DS-RBGX-GS2; (d) DS-RBGX-GS3.

5.3. Model verification

To ensure the precision of the numerical model, the numerical results are compared with experimental results. As illustrated in Fig. 11, the shell-side pressure drop Δp_s and heat transfer coefficient h_s are designated to characterize the performance of the DS-RBHX. Qualitatively, both Δp_s and h_s of numerical results present the same behaviors with those of experiments. The deviations between the numerical and experimental results keep around 10% and 15%, respectively. More specifically, the deviations of Δp_s vary from 11.6% to 8.9%, while those of h_s change from 19.0% to 14.0%. In general, the deviations are deemed to be reasonable for STHXs. Therefore, the numerical model, employed in this study, is effective and accurate.

5.4. Effects of guide shell on shell-side performance

Fig. 12 illustrates the path lines and velocity distributions of a longitudinal section of the outlet zone. From the comparison among four DS-RBHXs, the guide shells have effects on the fluid flow in different extent. All three guide shells play a positive role in reducing the flow dead zone. From Fig. 12, it can be found clearly that the DS-RBHX-GS2 has a more uniform and homogenous velocity distribution, particularly in the outer side of the outlet zone, than the DS-RBHX-GS1 and DS-RBHX-GS3. Consequently, it is logical to determine qualitatively and preliminarily that the guide shell of the DS-RBHX-GS2 have a better effect on the heat transfer enhancement of the outlet zone.

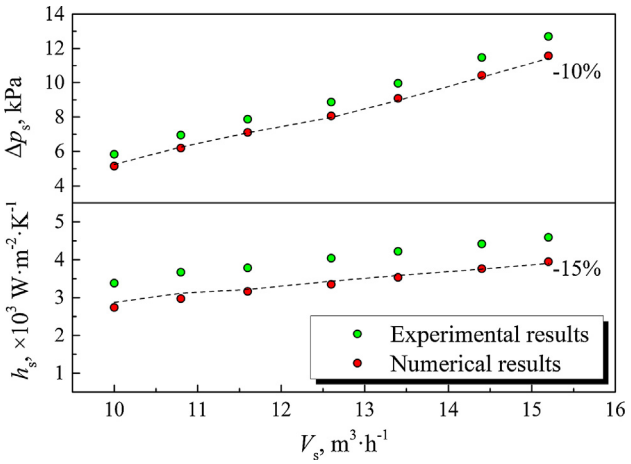

Fig. 11. Comparison between experimental and numerical results in shell side of DS-RBHX.

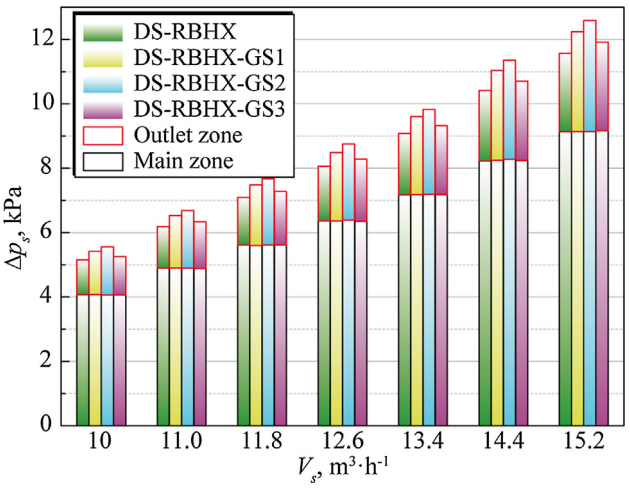

Fig. 13. Comparison of shell-side pressure drop among four DS-RBHXs.

The pressure drops in different zones among four DS-RBHXs are compared in Fig. 13. The guide shells, arranged in DS-RBHX-GS1, DS-RBHX-GS2, and DS-RBHX-GS3, only impact the performance of the outlet zone, while they have no effect on the main zone. Therefore, the pressure drop of the main zone keeps constant among four DS-RBHXs. However, for the outlet zone, the pressure drop of the DS-RBHX-GSs is higher than that of the DS-RBHX as listed in Table 5. It increases by around 26%, 39%, and 12% in the outlet zone for the DS-RBHX-GS1, DS-RBHX-GS2, and DS-RBHX-GS3, respectively. Meanwhile, relative to the DS-RBHX, the whole shell-side pressure drop rises by about 5.6%, 8.4%, and 2.6% for DS-RBHX-GS1, DS-RBHX-GS2, and DS-RBHX-GS3, respectively.

Effects of the guide shell on the heat transfer performance are depicted in Fig. 14 and Fig. 15. Similar to the pressure drop, the heat transfer rates of the main zone keep consistent for four DS-RBHXs according to Fig. 14. The heat transfer rates of the outlet zone for the four DS-RBHX are compared in Table 6. Compared with the DS-RBHX, those of the outlet zones increase by about 10%, 22%, and 7% for the DS-RBHX-GS1, DS-RBHX-GS2, and DS-RBHX-GS3, respectively. Fig. 15 presents the heat transfer coefficient of the shell side and outlet zone. It is evident that the heat transfer coefficient keeps the same pace with the heat transfer rate. The heat transfer coefficients of the outlet zone of the DS-RBHX-GS1, and DS-RBHX-GS2, and DS-RBHX-GS3 are around 11%, 23%, and 7% higher than those of the DS-RBHX. Meanwhile, with respect to the shell-side heat transfer coefficient, the increments are 1.1%, 2.6%, and 0.7%, respectively. As a result, the guide shell exerts the significant and positive influence on the shell-side outlet zone. Furthermore, the influence is fairly slight for the whole shell side, because that the main zone predominates in the shell-side heat transfer performance.

The heat transfer rates of the inner side and outer side in the outlet zone are compared in Fig. 16. For the inner side, the heat transfer rates of GS-RBHX-GS1 and GS-RBHX-GS2 are around 4% and 5% higher than that of the DS-RBHX, respectively, while an unfavorable effect, a decrease of 8%, occurs on the DS-RBHX-GS3. For the outer side, the heat transfer rates of DS-RBHX-GS1, DS-RBHX-GS2, and DS-RBHX-GS3 increase by 13%, 29%, and 13%, respectively. On account of the decline of the heat transfer performance of the inner side in the outlet zone of the DS-RBHX-GS3, the effect of the guide shell of DS-RBHX-GS3 is weaker than the others.

To further investigate the effects of guide shells, the local heat fluxes of the inner side and outer side of the outlet zone in four DS-RBHXs, at shell-side volume flow rate V_s = 12.6 m^3/h, are exemplarily compared in Fig. 17. Contrasting Fig. 12 and Fig. 17, the local heat fluxes keep unanimous with the velocity distributions. For

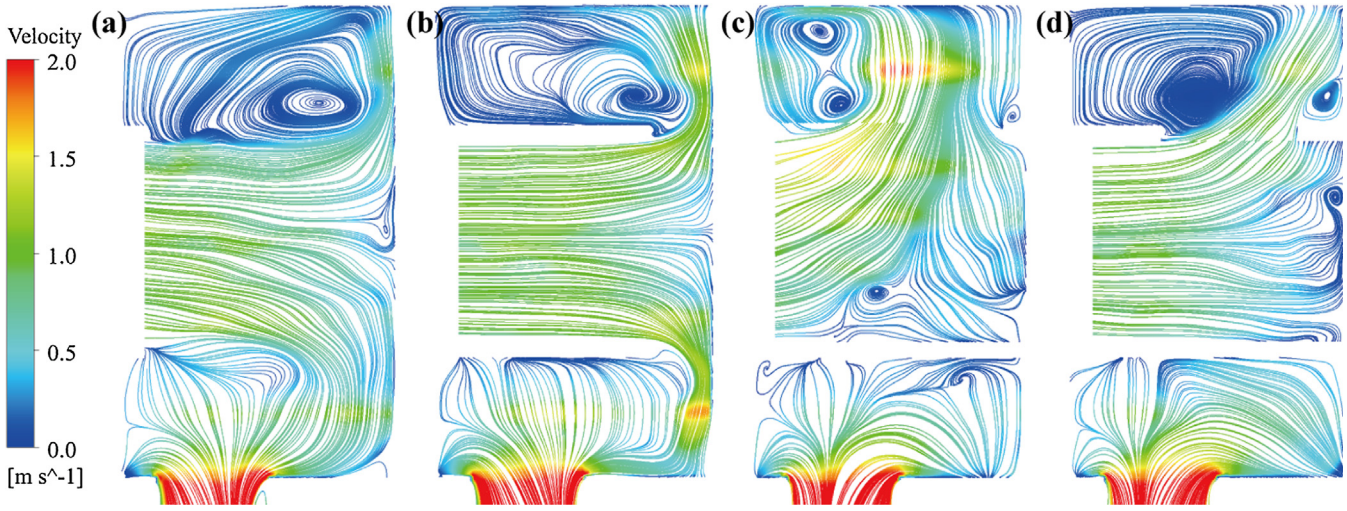

Fig. 12. Comparison of path lines and velocity distribution among four DS-RBHXs: (a) DS-RBHX; (b) DS-RBHX-GS1; (c) DS-RBHX-GS2; (d) DS-RBHX-GS3.

Table 5
Pressure drops of outlet zone for four DS-RBHXs.

V_s, m^3/h	$\Delta p_{s\text{-}oz}$, kPa			
	DS-RBHX	DS-RBHX-GS1	DS-RBHX-GS2	DS-RBHX-GS2
10.0	1.085	1.349	1.493	1.200
11.0	1.302	1.635	1.799	1.454
11.8	1.482	1.878	2.067	1.663
12.6	1.695	2.125	2.361	1.920
13.4	1.912	2.420	2.637	2.142
14.4	2.192	2.785	3.089	2.473
15.2	2.434	3.101	3.448	2.755

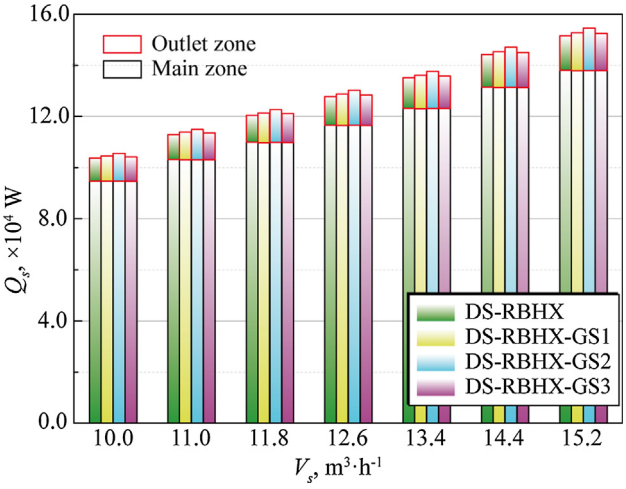

Fig. 14. Comparison of shell-side heat transfer rate among four DS-RBHXs.

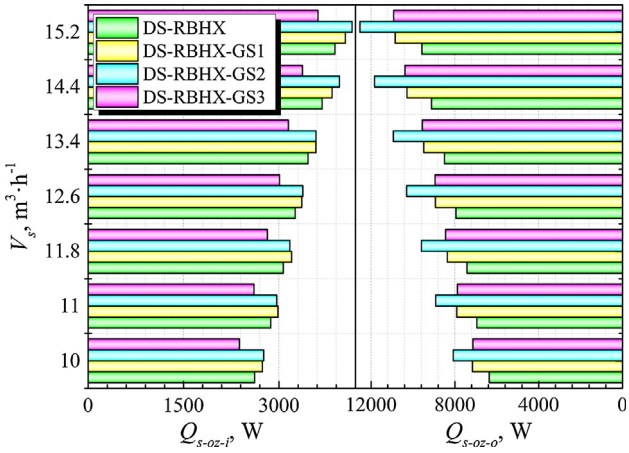

Fig. 16. Variation of heat transfer rate in inner side and outer side of guide shells in outlet zone.

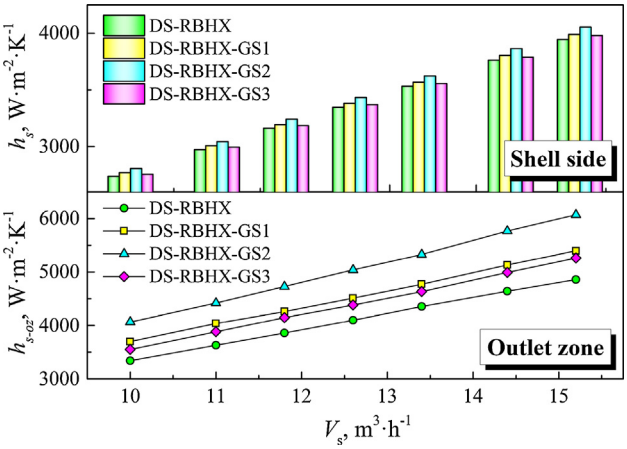

Fig. 15. Heat transfer coefficient of shell side and outlet zone versus shell-side volume flow rate.

instance, Fig. 12(d) shows that, in the outlet zone of the DS-RBHX-GS3, the working fluid flows into the outer side from the inner side via rectangular openings in the guide shell. At the same time, the flow velocity of the inner side declines. As a result, as depicted in Fig. 16 and Fig. 17, the heat transfer rate and heat flux of the inner side in the outlet zone of the DS-RBHX-GS3 are lower than those of the DS-RBHX. For the outer side, Fig. 12 clearly show that the flow velocities of the DS-RBHX-GS2 are higher and more well-distributed than those of the other three DS-RBHXs. Consequently, the local heat fluxes of the outer side in the outlet zone of the DS-RBGX-GS2, as illustrated in Fig. 17, are obviously high and steady as well. As a final example, the local heat fluxes of the outer side rise considerably at the end of the outlet zones of the DS-RBHX, DS-RBHX-GS1, and DS-RBHX-GS3 in Fig. 17, which also keeps consistent with the velocity distribution described in Fig. 12 (a), (b), and (d), respectively.

Fig. 18 illustrates the variation of heat transfer rate with respect to the power consumption in the shell-side outlet zone for four DS-RBHXs. From Fig. 18, it can be clearly observed that the heat trans-

Table 6
Heat transfer rates of outlet zone for four DS-RBHXs.

V_s, m^3/h	$Q_{s\text{-}oz}$, ×10^4 W			
	DS-RBHX	DS-RBHX-GS1	DS-RBHX-GS2	DS-RBHX-GS3
10.0	0.8973	0.9903	1.0843	0.9526
11.0	0.9823	1.0897	1.1884	1.0488
11.8	1.0491	1.1559	1.2766	1.1258
12.6	1.1205	1.2291	1.3675	1.1958
13.4	1.1952	1.3063	1.4518	1.2699
14.4	1.2799	1.4118	1.5786	1.3746
15.2	1.3449	1.4893	1.6678	1.4536

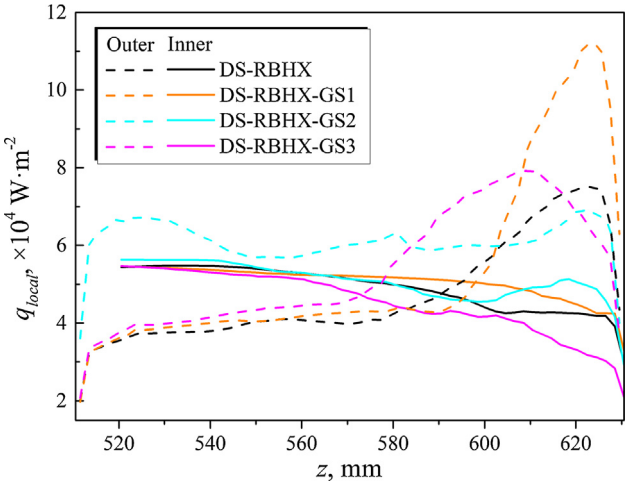

Fig. 17. Comparison of local heat flux in outlet zone among four DS-RBHXs.

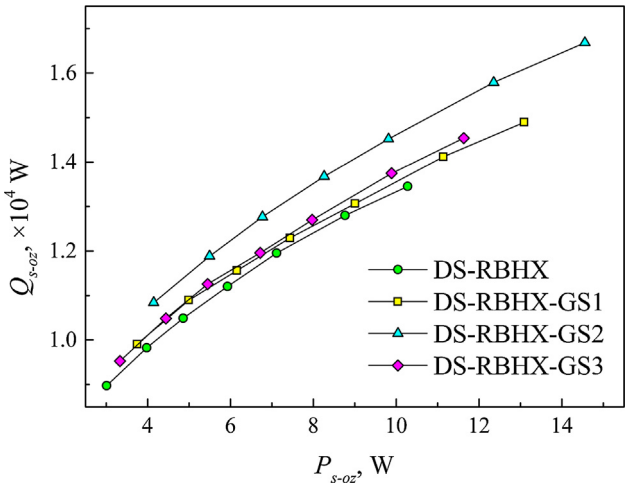

Fig. 18. Heat transfer rate versus power consumption in shell-side outlet zone.

fer rate of three DS-RBHX-GSs is higher than that of the DS-RBHX under the same pump cost. Among three DS-RBHX-GSs, DS-RBHX-GS2 gains the highest heat transfer rate under the same power consumption for all given working conditions. Under the same power consumption, the heat transfer rate of the DS-RBHX-GS2 increases by around 9% than that of the DS-RBHX. Therefore, guide shells absolutely play a positive part in improving the overall performance of the outlet zone. Likewise, DS-RBHX-GS2 present the best comprehensive performance in the shell-side outlet zone.

To sum up, all three guide shells have positive effects on the heat transfer enhancement of the outlet zone, especially in the outer side. More specifically, the guide shell of the DS-RBHX-GS2, the most effective one among three guide shells, makes the heat transfer coefficient and pressure drop increase by around 23% and 39% for the outlet zone, as well as 2.6% and 8.4% for the whole shell side, respectively. Instead, that of the DS-RBHX-GS3 has the weakest effect on the heat transfer performance.

6. Conclusion

In the present work, a double shell-pass rod baffle heat exchanger (DS-RBHX) is investigated experimentally and compared with a single shell-pass rod baffle heat exchanger (SS-RBHX). Likewise, three kinds of guide shells are proposed and arranged in the shell-side outlet zone of the DS-RBHX to reduce the flow dead zone and enhance the heat transfer performance. DS-RBHXs with different shell guides are compared with the DS-RBHX numerically. Finally, several conclusions are outlined as follows.

(1) The shell-side heat transfer coefficient of the DS-RBHX is dramatically improved. Compared with the SS-RBHX, under the same volume flow rate, it rises by 33.5–54.0%, while the shell-side pressure drop increases by 34.2–74.3%.
(2) From the perspective of the comprehensive performance, within the test scope, the shell-side heat transfer coefficient of the DS-RBHX is 14.4–24.3% higher than that of the SS-RBHX under the same shell-side pressure drop.
(3) All three guide shells have positive effects on the heat transfer enhancement of the outlet zone, especially in the outer side. The guide shell of the DS-RBHX-GS2 is the most effective one, while the effect of the guide shell in the DS-RBHX-GS3 is fairly slight.
(4) Guide shells have more effects on the outer side of the outlet zone than the inner side. Particularly, the guide shell of the DS-RBHX-GS3 plays a negative role in the heat transfer enhancement of the inner side. For the outer side, the heat transfer rates of DS-RBHX-GS1, DS-RBHX-GS2, and DS-RBHX-GS3 increase by 13%, 29%, and 13%, respectively. Therefore, the improvement of heat transfer performance of the shell-side outlet zone is attributed to the significant effects of guide shells on the outer side rather than the inner side.
(5) Compared with the DS-RBHX, the heat transfer coefficient and pressure drop of the outlet zone of the DS-RBHX-DS2 increase by 23% and 39%, while those of whole shell side merely rise by 2.6% and 8.4%, because the main zone plays a dominant part in the shell-side heat transfer performance.

As a final, it is proved experimentally that the DS-RBHX dramatically improve the heat transfer performance relative to the SS-RBHX. The guide shells are effective to enhance the heat transfer of the shell-side outlet zone although the effects are slight for the whole shell side of the DS-RBHX. Therefore, the DS-RBHX and DS-RBHX-GS both are the meaningful solutions for more efficient energy utilization.

Conflict of interest

The authors declared that there is no conflict of interest.

Acknowledgements

This work is financially supported by the Key Program of the National Natural Science Foundation of China (Grant No. 51736004) and National Key Research and Development Program of China (Grant No. 2017YFB0603501-3).

References

[1] E.U. Schlünder, K.J. Bell, D. Chisholm, G.F. Hewitt, F.W. Schmidt, D.B. Spalding, Heat Exchanger Design Handbook, Hemisphere Publishing Corporation, Washington; New York; London, 1983.
[2] Z.F. Huang, A. Nakayama, K. Yang, C. Yang, W. Liu, Enhancing heat transfer in the core flow by using porous medium insert in a tube, Int. J. Heat Mass Transf. 53 (2010) 1164–1174, https://doi.org/10.1016/j.ijheatmasstransfer.2009.10.038.
[3] A.W. Fan, J.J. Deng, A. Nakayama, W. Liu, Parametric study on turbulent heat transfer and flow characteristics in a circular tube fitted with louvered strip inserts, Int. J. Heat Mass Transf. 55 (2012) 5205–5213, https://doi.org/10.1016/j.ijheatmasstransfer.2012.05.023.

[4] X. Zhang, Z. Liu, W. Liu, Numerical studies on heat transfer and friction factor characteristics of a tube fitted with helical screw-tape without core-rod inserts, Int. J. Heat Mass Transf. 60 (2013) 490–498, https://doi.org/10.1016/j.ijheatmasstransfer.2013.01.041.
[5] J.F. Yang, Y.S. Lin, H.B. Ke, M. Zeng, Q.W. Wang, Investigation on combined multiple shell-pass shell-and-tube heat exchanger with continuous helical baffles, Energy 115 (2016) 1572–1579, https://doi.org/10.1016/j.energy.2016.05.090.
[6] J. Wen, H.Z. Yang, S.M. Wang, Y.L. Xue, X. Tong, Experimental investigation on performance comparison for shell-and-tube heat exchangers with different baffles, Int. J. Heat Mass Transf. 84 (2015) 990–997, https://doi.org/10.1016/j.ijheatmasstransfer.2014.12.071.
[7] H. Tang, Y. Chen, J. Wu, S. Yang, Numerical investigation of the performances of axial separation helical baffle heat exchangers, Energy Convers. Manage. 126 (2016) 400–410, https://doi.org/10.1016/j.enconman.2016.08.003.
[8] A. El Maakoul, A. Laknizi, S. Saadeddine, M. El Metoui, A. Zaite, M. Meziane, A. Ben Abdellah, Numerical comparison of shell-side performance for shell and tube heat exchangers with trefoil-hole, helical and segmental baffles, Appl. Therm. Eng. 109 (2016) 175–185, https://doi.org/10.1016/j.applthermaleng.2016.08.067.
[9] Y.H. You, A.W. Fan, S.Y. Huang, W. Liu, Numerical modeling and experimental validation of heat transfer and flow resistance on the shell side of a shell-and-tube heat exchanger with flower baffles, Int. J. Heat Mass Transf. 55 (2012) 7561–7569, https://doi.org/10.1016/j.ijheatmasstransfer.2012.07.058.
[10] M.M. Aslam Bhutta, N. Hayat, M.H. Bashir, A.R. Khan, K.N. Ahmad, S. Khan, CFD applications in various heat exchangers design: a review, Appl. Therm. Eng. 32 (2012) 1–12, https://doi.org/10.1016/j.applthermaleng.2011.09.001.
[11] J.F. Zhang, B. Li, W.J. Huang, Y.G. Lei, Y.L. He, W.Q. Tao, Experimental performance comparison of shell-side heat transfer for shell-and-tube heat exchangers with middle-overlapped helical baffles and segmental baffles, Chem. Eng. Sci. 64 (2009) 1643–1653, https://doi.org/10.1016/j.ces.2008.12.018.
[12] B. Gao, Q. Bi, Z. Nie, J. Wu, Experimental study of effects of baffle helix angle on shell-side performance of shell-and-tube heat exchangers with discontinuous helical baffles, Exp. Therm. Fluid Sci. 68 (2015) 48–57, https://doi.org/10.1016/j.expthermflusci.2015.04.011.
[13] Z.G. Zhang, M. Da Bin, F. Xiao Ming, G. Xue Nong, Experimental and numerical heat transfer in a helically baffled heat exchanger combined with one three-dimensional finned tube, Chem. Eng. Process. Process Intensif. 47 (2008) 1738–1743, https://doi.org/10.1016/j.cep.2007.09.012.
[14] Z.G. Zhang, T. Xu, X.M. Fang, Experimental study on heat transfer enhancement of a helically baffled heat exchanger combined with three-dimensional finned tubes, Appl. Therm. Eng. 24 (2004) 2293–2300, https://doi.org/10.1016/j.applthermaleng.2004.01.012.
[15] S. Renaud-Boivin, M. Poirier, N. Galanis, Experimental study of hydraulic and thermal behavior of an ice slurry in a shell and tube heat exchanger, Exp. Therm. Fluid Sci. 37 (2012) 130–141, https://doi.org/10.1016/j.expthermflusci.2011.10.014.
[16] B. Farajollahi, S.G. Etemad, M. Hojjat, Heat transfer of nanofluids in a shell and tube heat exchanger, Int. J. Heat Mass Transf. 53 (2010) 12–17, https://doi.org/10.1016/j.ijheatmasstransfer.2009.10.019.
[17] E.E. Wilson, A basis for rational design of heat transfer apparatus, ASME J. Heat Transfer 37 (1915) 47–70.
[18] B. Peng, Q.W. Wang, C. Zhang, G.N. Xie, L.Q. Luo, Q.Y. Chen, M. Zeng, An experimental study of shell-and-tube heat exchangers with continuous helical baffles, J. Heat Transfer 129 (2007) 1425, https://doi.org/10.1115/1.2754878.
[19] N. Jamshidi, M. Farhadi, D.D. Ganji, K. Sedighi, Experimental analysis of heat transfer enhancement in shell and helical tube heat exchangers, Appl. Therm. Eng. 51 (2013) 644–652, https://doi.org/10.1016/j.applthermaleng.2012.10.008.
[20] J. Fernandez-Seara, F.J. Uhía, J. Sieres, A. Campo, A general review of the Wilson plot method and its modifications to determine convection coefficients in heat exchange devices, Appl. Therm. Eng. 27 (2007) 2745–2757, https://doi.org/10.1016/j.applthermaleng.2007.04.004.
[21] K. Thulukkanam, Heat Exchanger Design Handbook, second ed., 2013. https://doi.org/10.1201/b14877.
[22] Q. Wang, M. Zeng, T. Ma, X. Du, J. Yang, Recent development and application of several high-efficiency surface heat exchangers for energy conversion and utilization, Appl. Energy 135 (2014) 748–777, https://doi.org/10.1016/j.apenergy.2014.05.004.
[23] C.C. Gentry, W.M. Small, Rod baffled heat exchanger, 4342360, 1982.
[24] C.C. Gentry, Rod baffle heat exchanger, 5139084, 1992.
[25] B.I. Master, K.S. Chunangad, A.J. Boxma, D. Kral, P. Stehlík, Most frequently used heat exchangers from pioneering research to worldwide applications, Heat Transfer Eng. 27 (2006) 4–11, https://doi.org/10.1080/01457630600671960.
[26] R. Smyth, A comparative assessment of RODbaffle shell-and-tube heat exchangers, Heat Transfer Eng. 2 (1981) 90–94, https://doi.org/10.1080/01457638108962763.
[27] Y. Qiu, M.J. Li, W.Q. Wang, B.C. Du, K. Wang, An experimental study on the heat transfer performance of a prototype molten-salt rod baffle heat exchanger for concentrated solar power, Energy 156 (2018) 63–72, https://doi.org/10.1016/j.energy.2018.05.040.
[28] J.J. Liu, Z.C. Liu, W. Liu, 3D numerical study on shell side heat transfer and flow characteristics of rod-baffle heat exchangers with spirally corrugated tubes, Int. J. Therm. Sci. 89 (2015) 34–42, https://doi.org/10.1016/j.ijthermalsci.2014.10.011.
[29] J. Yang, W. Liu, Numerical investigation on a novel shell-and-tube heat exchanger with plate baffles and experimental validation, Energy Convers. Manage. 101 (2015) 689–696, https://doi.org/10.1016/j.enconman.2015.05.066.
[30] X.T. Wang, N.B. Zheng, P. Liu, Z.C. Liu, W. Liu, Numerical investigation of shell side performance of a double shell side rod baffle heat exchanger, Int. J. Heat Mass Transf. 108 (2017) 2029–2039, https://doi.org/10.1016/j.ijheatmasstransfer.2017.01.055.
[31] R.W. Serth, Process Heat Transfer Principles and Applications, Elsevier Science and Technology Books, 2007.
[32] A.J. Wheeler, A.R. Ganji, Introduction to Engineering Experimentation, third ed., Upper Saddle River, New Jersey, 2010.
[33] J. Yang, L. Ma, J. Bock, A.M. Jacobi, W. Liu, A comparison of four numerical modeling approaches for enhanced shell-and-tube heat exchangers with experimental validation, Appl. Therm. Eng. 65 (2014) 369–383, https://doi.org/10.1016/j.applthermaleng.2014.01.035.
[34] E. Ozden, I. Tari, Shell side CFD analysis of a small shell-and-tube heat exchanger, Energy Convers. Manage. 51 (2010) 1004–1014, https://doi.org/10.1016/j.enconman.2009.12.003.
[35] ANSYS Inc, ANSYS FLUENT 15.0 User's Guide, 2013.